Article

Selection of Constitutive Material Model for the Finite Element Simulation of Pressure-Assisted Single-Point Incremental Forming

Ali Abdelhafeez Hassan [1,*] , **Gökhan Küçüktürk** [2] , **Hurcan Volkan Yazgin** [3] , **Hakan Gürün** [4]
and Duran Kaya [5]

1   Department of Engineering, School of Computing, Engineering and Digital Technologies, Teesside University, Middlesbrough TS1 3BX, UK
2   Department of Mechanical Engineering, Faculty of Engineering, Gazi University, Ankara 06560, Türkiye
3   Pi Makina, Gaziosmanpasa Mah. 97, 1 Sokak No: 6, Golbasi, Ankara 06830, Türkiye
4   Department of Manufacturing Engineering, Faculty of Technology, Gazi University, Ankara 06560, Türkiye
5   Department of Mechanical Engineering, Graduate School of Natural and Applied Sciences, Gazi University, Ankara 06560, Türkiye
*   Correspondence: a.hassan@tees.ac.uk

Abstract: Pressure-assisted single-point incremental forming (PA-SPIF) is one of the emerging forming techniques for sheet metals that have been the subject of rigorous research over the past two decades. Understanding of its forming mechanisms and capabilities is growing as a result. Open gaps are still present in material constitutive modelling for accurate numerical predictions and finite-element simulations as the characteristics of localised deformation behaviour in SPIF are different from those of conventional sheet metal forming. The current investigation focused on the comparison of three different material models for the finite-element analysis of PA-SPIF of cold-rolled, dual-phase steel DP600. Experimental trials using different fluid pressures showed good agreement with simulation results with discrepancies in deformed blank thickness and shape geometry predictions of 3–11% and 10–21%, respectively. Within the tested materials and range of parameters, the fracture-forming-limit diagram (FFLD) material model was identified to be of superior accord with experiments.

Keywords: incremental forming; finite element; sheet metal; damage model; pressure assisted; hybrid manufacturing

1. Introduction

Single-point incremental forming (SPIF) is a near-net-shape manufacturing process in which a simple tool follows a specific tool path to deform sheet metal into complex prototype parts with sufficient precision. It is considered as one of the hybrid manufacturing techniques that use CNC machine tools to deform metal sheet. The process has a high potential economic payoff for the production of complex sheet metal parts in small quantities while using simple tooling. SPIF is characterised by its high formability compared with conventional sheet-metal-forming techniques. The enhanced formability is mainly attributed to the localised forming, which changes the damage and fracture behaviours of metal sheet compared with conventional processes such as stamping and deep drawing [1]. While enhanced formability was reported for high-speed forming techniques such as electromagnetic forming [2–4], the superiority of SPIF lies in the precise control of deformed shape with simple tooling. Due to the lengthy manufacturing time per part, the SPIF method is best suited for prototypes or limited production runs. In the last 20 years, specifically, the SPIF approach has been a fascinating area of study for shaping lightweight materials in the aerospace and automotive sectors [5–9]. Different domains prefer SPIF procedures,

notably in the automobile industry. Important biological uses, such as cranial implants, have grown in recent years. The form of the human body must be taken into consideration when individually manufacturing medical implants for patients, which can be considered by utilising the advancement in medical imaging and CAD/CAM technologies. As a result, one of the SPIF applications that have received the greatest investigation is the creation of specialised medical implants such as skull plates, knee prostheses, face implants, and palate prostheses [10–14].

SPIF approaches have been extensively studied as the process shapes ferrous and nonferrous metals without dies. With SPIF, excessive thinning, geometry deviation, and surface-quality deterioration occur when shaping light, high-strength materials. To employ a technology that offers such flexible manufacturing in the industry, it is vital to research numerous parameters and properly understand the boundaries of the shape. Different sheet materials are shaped with single-point, two-point, and kinematic ISF methods, according to the findings. Due to their microstructure, which consists of dispersion of hard martensite particles in a soft and formable ferrite matrix, dual-phase (DP) steels are of tremendous importance to the automobile industry. This construction offers improved durability without sacrificing formability; however, because of their complex failure behaviour, their applications are limited [15].

Ham et al. [16] established the ISF shaping and effect ratio parameters. The study employed AA 3003 aluminium sheeting. The wall angle, form depth, spindle speed, and step-down size affected shaping. The depth and diameter did not affect the shape. The material thickness and tool diameter affected the wall angle more than the step-down size did. Afonso et al. [17] shaped tunnel portions (full and half-tunnel forms) with ISF. Two-millimetre-thick 1050-H111 aluminium was used. The feed rate was 1500 mm/min, and the tool diameter was 10 mm. The form correctness and greatest wall angle were tested. Up to 68° wall angle might be achieved within 5 mm. Moayedfar et al. [18] studied the effect of forming parameters during incremental sheet forming of 316 stainless steel. The findings indicated that as the spindle speed and feed rate grew, so did the sheet stretch, until the sheet could no longer stretch and the process shifted from forming to shear thinning. At greater spindle speed and feed rates, the surface quality suffered. Manco et al. [19] studied the impact of SPIF parameters on 6082-T6 aluminium alloy sheets formability. Using design of experiments and statistical analysis, they created a model to predict the final wall thickness based on the initial sheet thickness, wall angle, tool diameter, and step-down size. Mugendiran et al. [20] evaluated the formability and wall-thickness variation of the AA5052 aluminium alloy during SPIF, and it was demonstrated that the conical component is more formable than the truncated pyramid part. Bastos et al. [21] studied the effects of the tool feed rate on the SPIF of AA 1050, DP600, DP780, and DP1000. The size, tool diameter, initial wall thickness, and lubrication were constant. According to their experiments, increasing the feed rate reduced the formability and surface quality of dual-phase materials, while aluminium blanks were not affected. Azevedo et al. [22] studied the lubrication's effect on the SPIF of AA 1050 and DP780. It was concluded that SAE 30 and AL-M grease oils had a beneficial effect on aluminium 1050 surface quality, whereas Finarol B5746 and AS-40 oils are better for DP780. They reported that the greater the hardness of the material to deform, the lower the necessary lubricant viscosity required. Ham et al. [23] studied SPIF dimensional accuracy based on the material type, thickness, form type, tool diameter, and step-down size. Conical, pyramidal, and dome-shaped aluminium 5754, 6451, and 5182 were used. Laser-scanned parts were compared with CAD designs for geometric accuracy. It was shown that the accuracy of the deformed final geometry is a function of the wall angle in addition to process parameters. Zhu et al. [24] proposed an algorithm for producing flat-walled parts that cannot be produced with conventional SPIF via adapting the tool path and sheet posture. The algorithm was reported to enhance the thickness uniformity of the final deformed parts [25]. Zhan et al. [26] introduced a new numerical–analytical model to disclose the thickness fracture mechanism and estimate the fracture limit during incremental forming. It was concluded that the fracture-forming limit with

increased speed tool rotation is higher compared with that of the cases without tool rotation. Mirnia et al. [27] used the modified Mohr–Coulomb (MMC3) ductile fracture criterion to numerically study single-point incremental forming and found that fracture begins at the surface via microcracks. It was deduced that the deformation strategy (e.g., multistage or multipaths) is vital for delaying the damage evolution in the process. Chang et al. [28] developed three-sheet incremental forming (TSIF) where the surface quality and forming limit were superior to those of the conventional process for aluminium alloys AA2024 and AA7075 sheet materials.

One of the early investigations on the FEA of incremental forming was carried out by Eyckens et al. [29]. They studied the straining behaviour in the process using various material models of AA3003-O and digital image correlation. It was concluded that process parameters dictate the way the plastic deformation occurs, i.e., by through-thickness shear or rather by bending. Henrard et al. [30] demonstrated that the type of finite element, constitutive law, and identification procedure for the material parameters influenced force prediction in FEA. Essa and Hartely [31] numerically and experimentally investigated SPIF, and it was deduced that using a backing plate reduced the unintended sheet bending near the top of the outer cone location. In addition, usage of an additional kinematic support tool and modified end tool path lessened springback and decreased the pillow effect, respectively. Esmaeilpour et al. [32] confirmed that, in FEA, choosing the suitable material model was the utmost critical parameter when modelling the process. Yan et al. [33] numerically investigated multistage SPIF optimisation of aluminium AA3003-O. It was shown that the two-stage forming technique could significantly reduce the geometrical deviation, thickness variation, and forming time. Li et al. [34] investigated the tool path optimisation of induction heating-assisted SPIF using machine learning. Material formability and surface quality were improved following the optimisation of the tool path and using machine learning; however, noticeable oxidation and alpha layer of the sheet material at heating temperature ~1040 °C were reported, and they were eliminated at ~950 °C. Frikha et al. [35] explored incremental forming of grade 2 α titanium for biomedical application (hip cup prostheses). The research suggested a novel multistep process in which a deep drawing was used for the spherical cup part, whereas incremental forming was used for the outer flange part. The low material formability was enhanced, and geometric accuracy has been improved. Wang et al. [36] proposed a novel algorithm for thickness prediction in SPIF using shape geometry and surface spline (NURBS). It was presented that the proposed algorithm is robust for predicting the thickness of formed parts when compared with experimental results and FE simulated ones. The algorithm was superior to the sine law when predicting the thicknesses of variable curvature surfaces. Pepelnjak et al. [37] depicted that reducing the computational time and effort is possible through optimising mass scaling of the material and element size of the FE mesh. The optimisation was achieved via artificial neural networks applied to the results obtained from FEA and compared with the experimental results for incremental forming of the DC04 steel.

Numerical simulation is the main tool for better understanding of the process while reducing the amount of experimental trials and the associated cost. The literature on FE analysis of pressure-assisted single-point incremental forming (PA-SPIF) is limited with none devoted for the identification of the suitable and most accurate material damage model to predict material failure during the process. Hence the current investigation focused on FE analysis of the PA-SPIF of the DP600 steel by comparing the performance of different material models in predicating workpiece deformation when contrasted to experimental trials. Combined with the material tensile stress–strain empirical relation, three damage models were compared, namely the Gurson–Tvergaard–Needleman, ductile, and fracture-forming-limit damage models. Then the material model with the highest accuracy to predict deformation was reported.

2. Materials and Methods

2.1. Experimental Work

In order to investigate the influence that the PA-SPIF process has on the formation of sheet metal, an experimental setup was created. Fluid pressure is applied in the opposite direction of the surface that is being formed by the sheet material. Through the use of this apparatus, it is possible to conduct experiments both with and without the application of pressure to the fluid. The experimental arrangement allows for the fluid pressure that is applied to the sheet material to be changed in a number of different ways. Figure 1 depicts the experimental setup that has been used and the process parameters. A MICROCUT Challenger 2412 CNC machine (maximum spindle speed of 8000 rpm and spindle power of 7.5 kW) was used for the trials. Experiments involving incremental sheet forming were conducted by utilising three different pressure settings: no pressure, 0.2 bar, and 0.4 bar. The fluid used for the trials was a mixture of water and Quakercool 7101 BFF lubricant (the ratio of water to lubricant volume was 20:1).
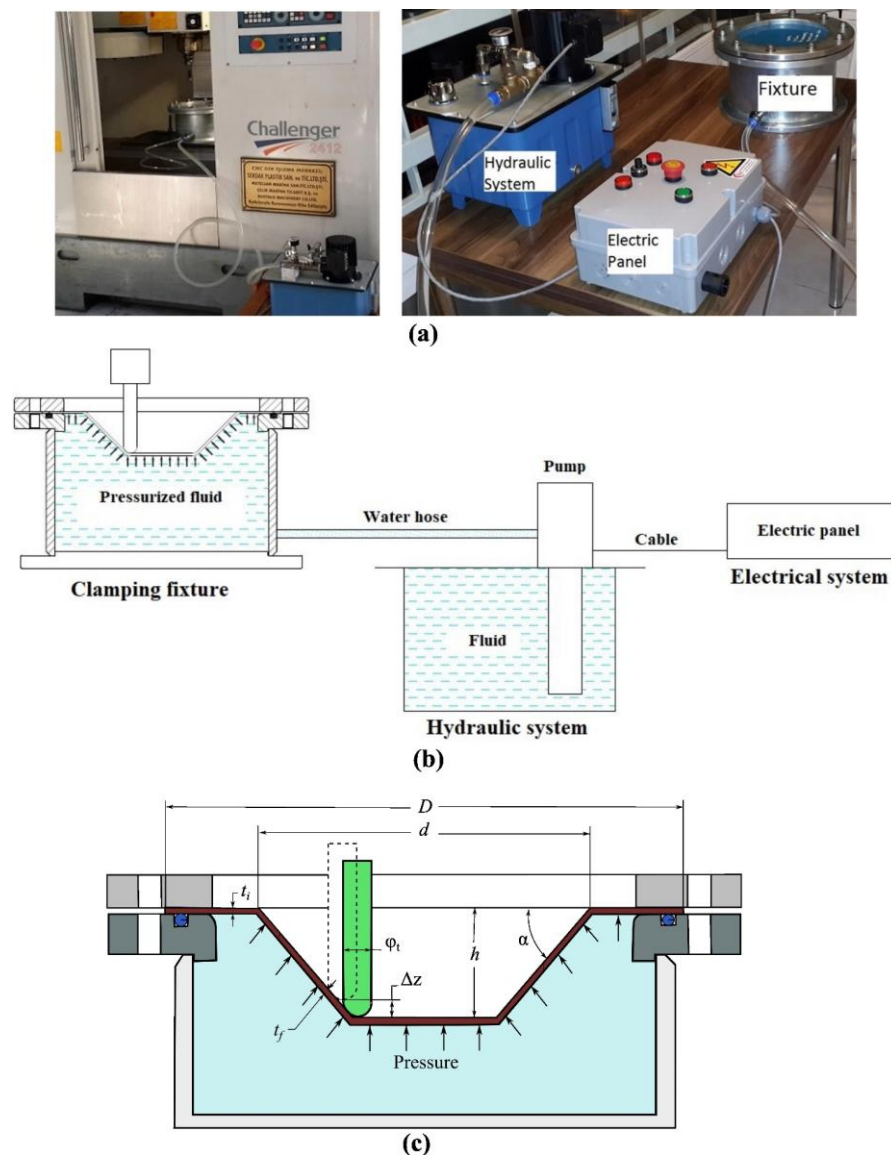

Figure 1. Experimental setup (**a**), detailed schematic of the setup (**b**), and process parameters (**c**).

Using Computer Aided Manufacturing (CAM), the processing G-codes were extracted and sent to the CNC machine in order to deform the sheet material into the desired shape. A

three-axis CNC vertical milling machine was utilised to mount the experimental equipment. The tool rotation direction is clockwise, speed is 800 rpm, machining direction is counter-clockwise, step-down size is $\Delta z = 0.5$ mm, and feed rate is 1000 mm/min. The forming tool is an SAE 430B manganese bronze alloy with a 16 mm diameter and a spherical end. For sheet material with a thickness of $t_i = 0.7$ mm and a diameter of D = 285 mm, the forming diameter is d = 180 mm, form height is h = 50 mm, and forming angle is $\alpha = 45°$. To assure accuracy, all experiments and measurements were repeated three times, and the average of the results was calculated. Due to the high manganese content of this tool, its resistance to wear is exceptional. Figure 2 depicts the utilised forming tool, whereas Table 1 outlines its elemental composition.

Figure 2. SAE 430B forming tools.

Table 1. Composition of forming tool and workpiece as well as properties of oil used.

	Al	Fe	Ni	Mn	Cu	Zn	Pb	Sn
Tool elemental composition (wt.%)	5.0	2.0	1.0	2.5	60	22	0.20	0.20
Oil physical Properties	Density (gr/cm^3)		Viscosity (mm^2/s)at 40 °C			Flash point (°C)		
	0.92		6			310		
Workpiece elemental composition (wt.%)	C	Mn	Si	Cr	Al	Ni	P	Cu
	0.116	1.545	0.289	0.634	0.042	0.041	0.029	0.019

Lubrication is required in the SPIF process to reduce friction-induced wear, enhance formability, and prolong tool life [38]. Before the experimental research, trial studies with various oil materials were conducted. According to studies on lubrication found in the scientific literature, the oils recommended for DP series materials have a low viscosity [39]. For this reason, research was pursued using a less viscous ester-based metal cutting oil. The oil of the brand CONDAT Condalu 200 was selected as the lubricant. In order to maintain consistent conditions, roughly 100 cm^3 of this oil was utilised in each experiment. Table 1 provides the physical properties of the used oil. Dual-phase DP600 sheet material, which has recently become popular in the automotive industry, has been selected as a sheet

material due to its high strength and superior formability. Figure 3 depicts the results of the tensile test conducted on the sheet material (thickness of 0.7 mm) used in the studies, whereas Table 1 details its chemical composition. A laser 3D scanner with the associated software used to scan the deformed sheet geometry is depicted in Figure 4 and obtains digital cloud surfaces of the workpiece. The laser scanning approach yields precise values with a resolution of 0.01 mm. The software Geomagic Verify™ was used to process the cloud surfaces and compare with the CAD of intended geometry.
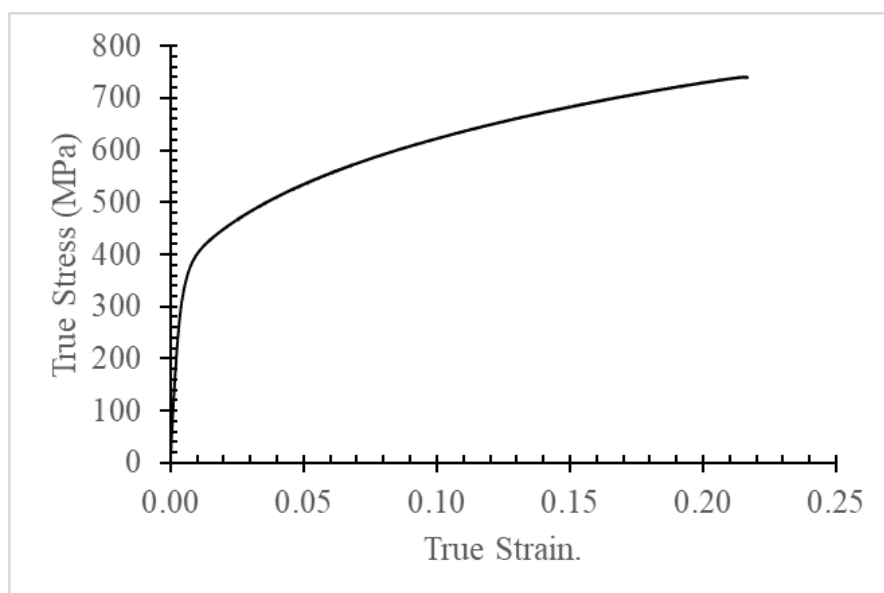

Figure 3. Experimental tensile stress–strain relation of DP600 steel (workpiece material).

Figure 4. Laser 3D scanner with its associated software.

2.2. FE Modelling Work

Finite-element analysis of PA-SPIF of DP600 steel blanks was carried out to understand various material models' effects on deformation prediction accuracy at three fluid pressure settings. The forming tool was developed as an analytical rigid body, with only the tool hemispherical tip and 10 mm of the tool shank considered. The blank was modelled as a deformable 3D continuum homogenous shell with a thickness of 0.7 mm. Simpson's integration rule was used during the analysis with 9 integration points over the thickness

to calculate the cross-sectional behaviour of the shell. The blank was meshed with S4R elements (4-node doubly curved, thin, reduced integration shell element) of 3 mm average size totalling 6820 elements. Figure 5 details the tool geometry, model assembly, and undeformed mesh of the blank.
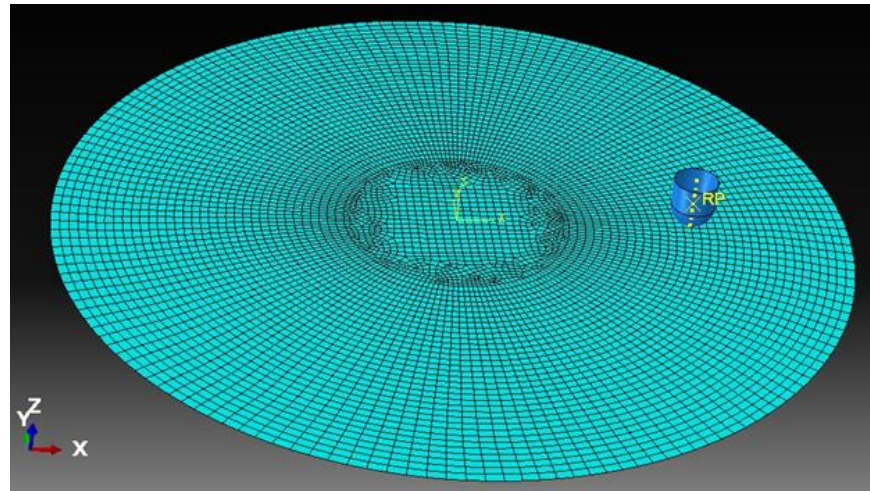

Figure 5. Model assembly and undeformed mesh.

Surface-to-surface contact was used to model the contact behaviour between the tool and blank. The friction coefficient between the tool and blank during SPIF is a function of process parameters as well as forming depth. Friction coefficient values ranging between 0.1 and 0.3 were reported during SPIF of the DP780 steel using various lubricants [22]. Therefore, an average friction coefficient value of 0.2 was considered for the tangential contact behaviour between the tool and blank in the model. The tool path used for experimental trials was inputted to the model as a displacement boundary condition of the tool to deform the blank to the required geometry. The outer perimeter of the blank was fixed, and the bottom outer surface (ring-shaped) of the blank was restricted from moving in the Z direction to represent the die and clamp plate restrictions on the blank. The fluid pressure was applied as a pressure load on the bottom surface of the blank. A dynamic explicit integration scheme was used with automatic time-increment calculation. The step total time period was 160 s, and no mass or time scaling was used. The blank material density is 7870 kg/m^3, while its Poisson's ratio and modulus of elasticity are 0.29 and 207 GPa, respectively. The material plastic behaviour obtained from experimental tensile tests was inputted to the model as tabulated values of plastic stress–strain paired values. Three material damage models were considered, namely the Gurson–Tvergaard–Needleman (GTN) damage model, ductile damage model, and fracture-forming-limit damage (FFLD) model. The GTN yield function is defined as in Equation (1).

$$\left(\frac{\sigma_{eq}}{\sigma_y}\right)^2 + 2q_1 f^* . \cosh\left(\frac{3q_2\sigma_m}{2\sigma_y}\right) - \left(1 - q_3 f^{*2}\right) = 0 \tag{1}$$

where σ_{eq} and σ_m are the equivalent von Mises stress and hydrostatic stress, respectively. q_1, q_2, and q_3 are the material parameters, and σ_y is the flow/yield stress of the material. The volume void fraction is modified to f^* due to the accelerating effects of the void coalescence as follows:

$$f^* = \begin{cases} f & , f \leq f_c \\ f_c + \frac{\frac{1}{q_3}\left(q_1 + \sqrt{q_1^2 - q_3}\right) - f_c}{f_f - f_c}(f - f_c) & , f_c < f < f_f \end{cases} \tag{2}$$

where f_c and f_f are the critical void volume fraction at the onset of voids coalescence and the critical void volume fraction at the onset of failure, respectively. The change in the void

volume fraction is due to the enlargement of existing voids and the nucleation of new voids. Thus, the rate of change in the void volume fraction is expressed as a sum of the rate of growth of existing voids (f_G) and the rate of void nucleation (f_N) and can be defined as in Equations (3) and (4).

$$\dot{f}_G = (1 - f^*).\dot{\varepsilon}^p{}_{kk} \tag{3}$$

$$\dot{f}_N = \frac{f_N}{S_N\sqrt{2\pi}} \exp\left(-\frac{1}{2}\left(\frac{\varepsilon^p_{eff} - \varepsilon_N}{S_N}\right)\right).\dot{\varepsilon}^p_{eff} \tag{4}$$

where $\dot{\varepsilon}^p{}_{kk}$ and $\dot{\varepsilon}^p_{eff}$ are the plastic hydrostatic strain rate and effective plastic strain rate, respectively. ε_N represents the mean nucleation strain with a standard deviation of S_N, and f_N is the void volume fraction of the nucleating voids. The DP600 steel parameters for the GTN model were collected from the literature [40] as detailed in Table 2.

Table 2. GTN model parameters [40].

q_1	q_2	q_3	f_0	f_c	f_f	f_N	S_N	ε_N
1.5	1	2.25	0.008	0.15	0.25	0.00062	0.1283	0.5421

The ductile damage (DD) criterion is a phenomenological model for predicting the onset of damage due to nucleation, growth, and coalescence of voids. The ductile damage model assumes that the fracture strain is a function of stress triaxiality (η), strain rate, and temperature. Stress triaxiality is a function of the hydrostatic stress (σ_h) and the equivalent von Mises stress (σ_{eq}) as defined by equation 5. The experimentally measured values of the fracture initiation strain at different triaxialities [41] are depicted in Figure 6; the associated data were inputted to the model as tabulated values, and a strain rate of 1 s^{-1} was considered to be a suitable average value for incremental-forming processes [42]. The aforementioned fracture strain represents the start or onset of material damage (strain at the start of fracture), which is followed by material damage evolution. A generalised model that relates triaxiality to equivalent initial fracture strain ($\bar{\varepsilon}^{pl}_0$) is depicted in Equation (6), with C_1 and C_2 as the material constants, and η_0 is generally approximated to be 0.333 [43].

$$\eta = \frac{\sigma_h}{\sigma_{eq}} = \frac{\frac{1}{3}(\sigma_1 + \sigma_2 + \sigma_3)}{\sqrt{\frac{1}{2}\left((\sigma_1 - \sigma_2)^2 + (\sigma_2 - \sigma_3)^2 + (\sigma_3 - \sigma_1)^2\right)}} \tag{5}$$

$$\bar{\varepsilon}^{pl}_0 = \begin{cases} \infty & , \eta \leq -\frac{1}{3} \\ \frac{C_1}{1+3\eta} & , -\frac{1}{3} \leq \eta \leq 0 \\ C_1 + (C_2 - C_1)\left(\frac{\eta}{\eta_0}\right)^2 & , 0 \leq \eta \leq \eta_0 \\ C_2\frac{\eta_0}{\eta} & , \eta_0 \leq \eta \end{cases} \tag{6}$$

In the damage evolution stage, the yield stress softens and elasticity degradation occurs until the material reaches a complete fracture when the material damage parameter (D) reaches 1 (see Figure 7). The material damage (D) in such a stage can be modelled as a function of the material fracture energy (G_f), effective plastic displacement (u^{pl}), and yield stress (σ_y) as detailed in Equation (7). The fracture energy for the DP600 steel was reported as 106 MJ/m^2. Compared with the extrapolated stress–strain relation following damage initiation, stresses during the damage evolution are softened or reduced by a factor of 1-D. To capture the residual load-carrying capability of a cracked ductile material, a postpeak softening component of the stress–strain curve is usually included in the modelling work.

$$D = 1 - \exp\left(-\int_0^{u^{pl}}\left(\frac{\sigma_y\,\dot{u}^{pl}}{G_f}\right)\right) \tag{7}$$
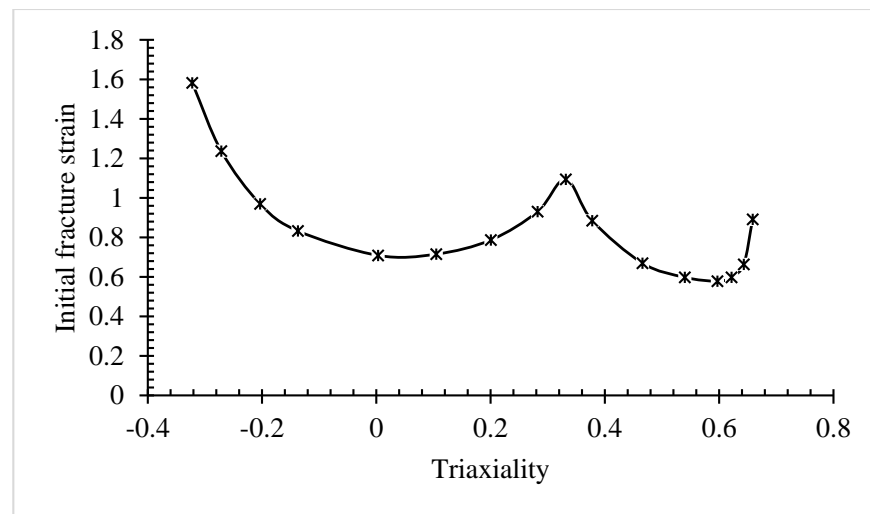
Figure 6. Fracture strain and triaxiality relation for DP600 steel.
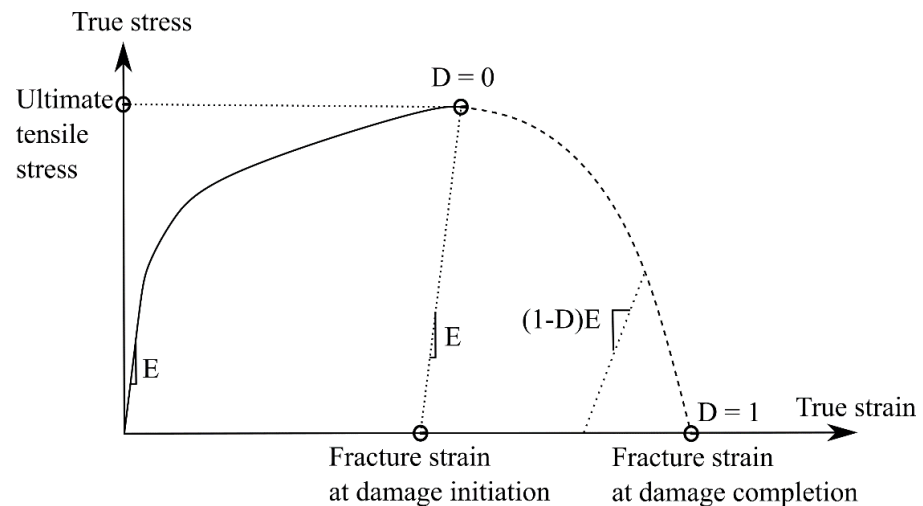

Figure 7. Typical stress–strain curve showing strain hardening and softening post damage initiation.

The basic necessity in every sheet-metal-forming operation is to evaluate the material's formability in order to achieve the desired shape without failure or fracture. Normally, the thickness of the sheet is much smaller than the other dimensions of the sheet that are responsible for selecting the plane stress condition. As a result, minor and major strains are employed to assess the formability of the material. The major and minor stresses in the necking zone are typically represented on a graph as a V-shape curve under different loading trajectories. This curve, known as the forming-limit diagram, defines the formability limit of sheet material without necking (FLD). When there is evident necking in the material during forming, FLD is applied. FLD is constructed around the strains in the necking zone. Some materials undergo instantaneous fracture without evident necking during processing; in such circumstances, formability is determined by assessing fracture strains at different loading trajectories and constructing the fracture-forming-limit diagram (FFLD). Following experimental trials, the fracture-forming-limit diagram for the DP600 sheet steel was reported by Habibi et al. [15]. The FFLD data used are depicted in Figure 8 and were entered to the model as tabulated FLD values. The damage evolution criterion (Equation (7)) was used in combination with FFLD to model the material behaviour during damage initiation and evolution.
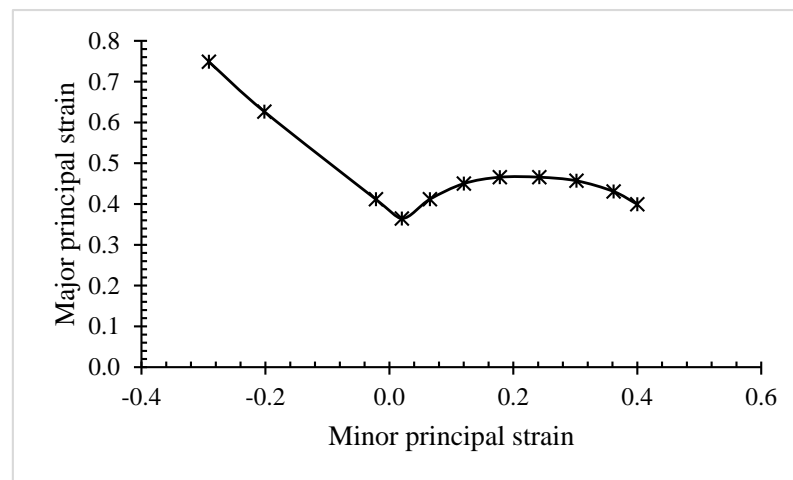
Figure 8. FFLD of DP600 steel.

3. Results and Discussion

Using laser scanning, changes in wall thickness and deviations from CAD data were measured on shaped sheet materials produced from experimental research with a resolution of 0.01 mm. Wall-thickness change and deviation readings from CAD data were measured at 10 mm intervals over the truncated cone height (from top to bottom). As demonstrated in Figure 9, PA-SPIF resulted in higher thinning than SPIF with the thinning increased when the pressure values grew. The fluid pressure acted as flexible die under the blank while it was being deformed. Therefore, the fluid pressure contributed to the squeezing or thinning of the metal sheet under the tool loading above and the fluid pressure below. This increased thinning of the blank thickness helped to reduce the springback effects by fully plasticising the sheet thickness. The springback of sheet metals in forming operations usually happens due to the residual elastic region across the sheet thickness after deformation [44]. The more plastic deformation delivered to the blank, the less springback was measured, and, thus, the less deviation from the intended final deformed geometry (CAD) of the blank. Figure 10 depicts the deviation from CAD of the final deformed blanks under different pressure settings. It is evident that, for higher pressure, the deviation is lower, which, as detailed earlier, could be attributed to higher plastic deformation across the sheet thickness with higher pressure and thus less springback or deviation. This increased plastic deformation effect was evident from the higher thinning of the blank with higher pressure.

Figure 11 depicts the deformed mesh of the model at different stages of deformation with no visible element shape distortion, which usually indicates a meshing problem by choosing the wrong element size, shape, and/or distribution. Figures 12–14 depict the von Mises stress distribution at the end of the process for different pressure settings and different material models. The material fracture (or element deletion) at the bottom or end bend of the cone, marked with a red arrow in Figure 13, was predicted by simulations that utilised a GTN material model, which was in contrast to an experimental work where no fracture was reported. However, in general, fractures usually occur near or at the bottom bend where the sidewall meets the bottom surface when forming truncated cones using SPIF. In addition, all the three material models predicted the maximum stress to be at the bottom bend. This can be attributed to the increased blank stretching and thickness thinning with tool advancement to the bottom surface to form the required shape. The predicted von Mises stress distribution and extremes for the three material models were dissimilar for different material models with discrepancies up to 100 MPa as shown in Figures 12–14. This highlights the importance of not only the plastic stress–strain relation but also the material damage model when simulating metal-forming processes and specially SPIF.
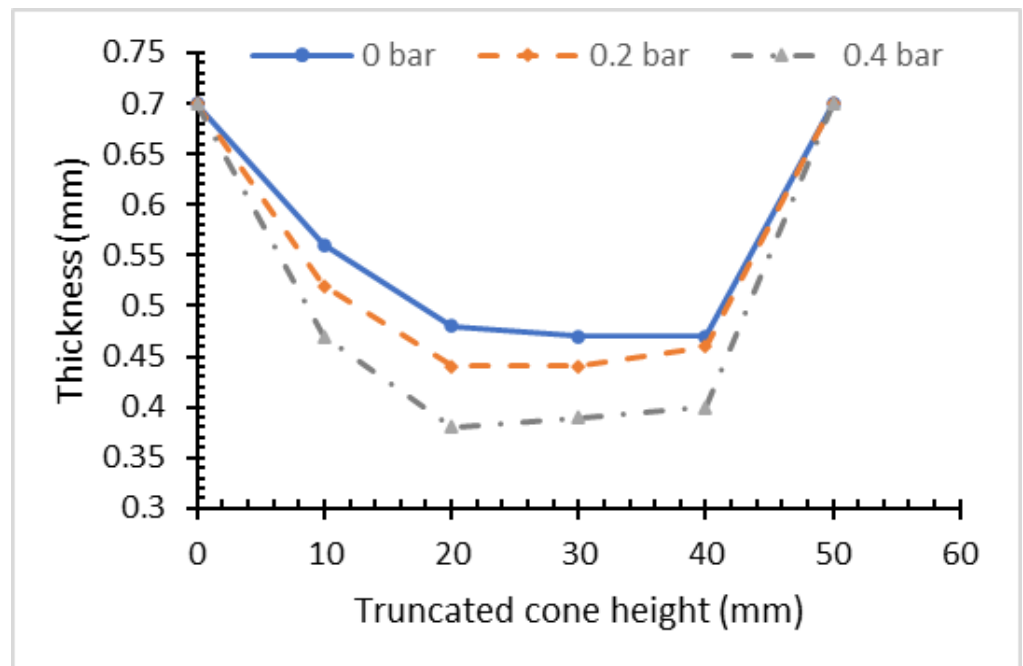
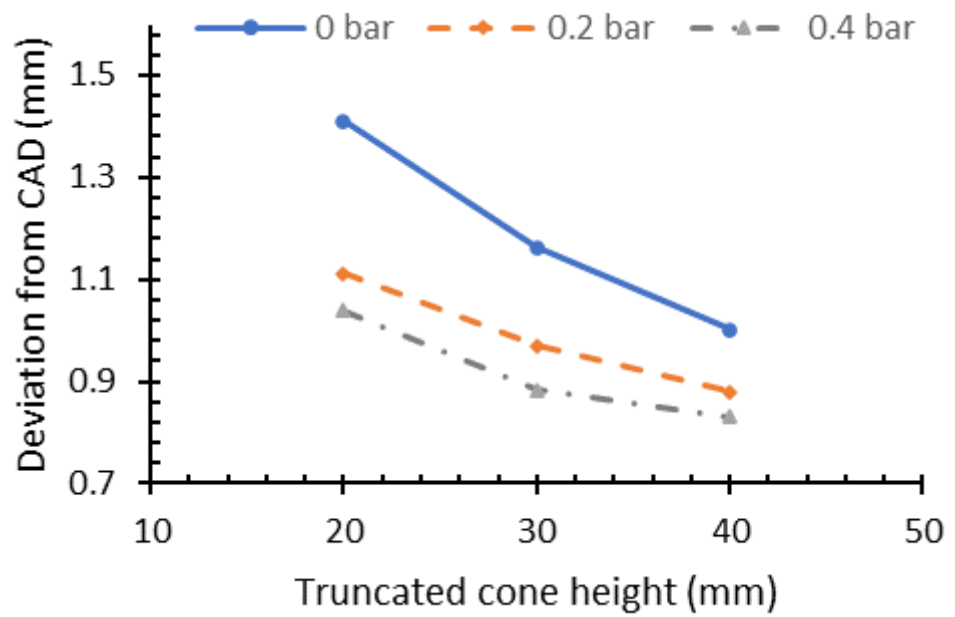**Figure 9.** Thickness variation of deformed blank at different pressure settings.

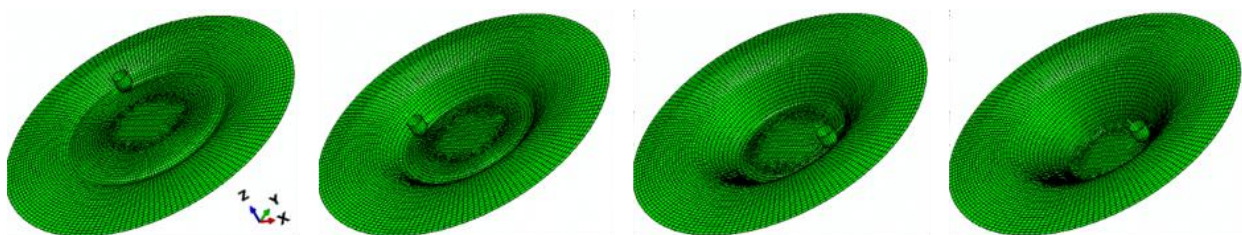**Figure 10.** Deviation from CAD of deformed blanks.

Figure 11. Blank deformation and deformed mesh over various stages (initial stage on left and final stage on right) of PA-SPIF.
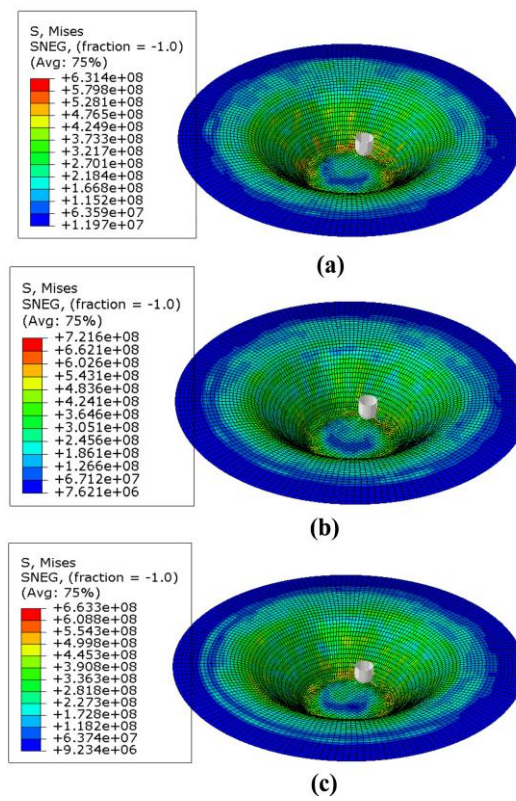
Figure 12. von Mises stress distribution for FFLD material model at (**a**) no fluid pressure, (**b**) pressure 0.2 bar, and (**c**) pressure 0.4 bar.
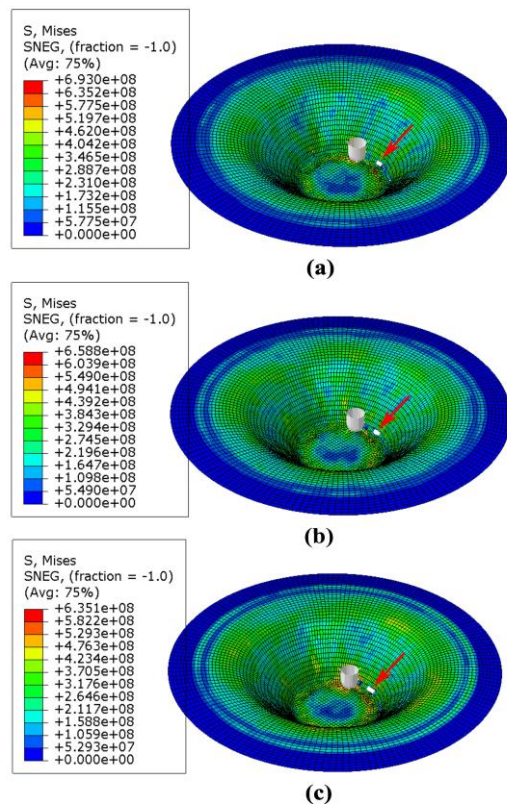

Figure 13. von Mises stress distribution for GTN material model at (**a**) no fluid pressure, (**b**) pressure 0.2 bar, and (**c**) pressure 0.4 bar. Predicted fracture regions are marked with red arrow.
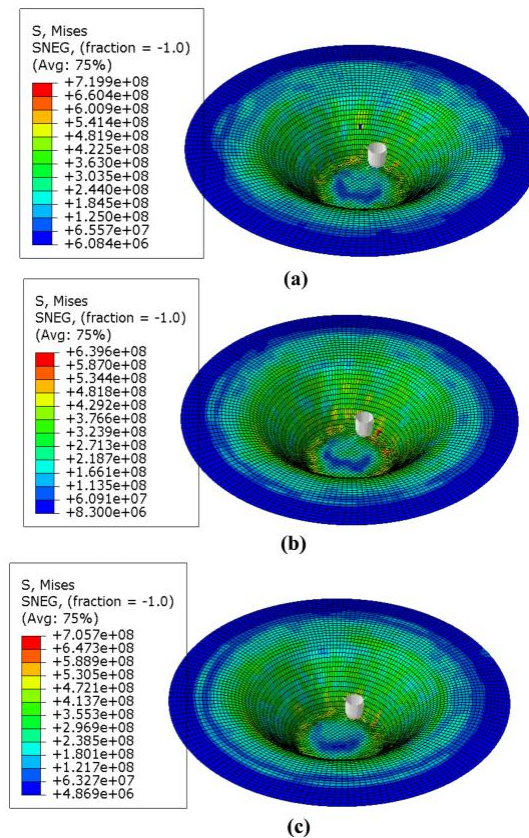
Figure 14. von Mises stress distribution for DD material model at (**a**) no fluid pressure, (**b**) pressure 0.2 bar and (**c**) pressure 0.4 bar.

Figure 15 shows the predicted final thickness of the deformed blank at different pressures and using the three material models. The data appeared to follow the same trend with experimental measured thickness where the thickness is reduced for the sidewalls of the cone compared with the top or bottom parts. The FFLD material model showed the least discrepancy from experimental work (up to 3%), whereas the GTN model showed the highest variation from measured thickness (up to 11%). This could be attributed to the drawbacks of the GTN model since it ignores fracture mechanisms brought on by shear, which might by an essential damage mechanism during SPIF [42]. Figure 16 illustrates the deviation from CAD for predicted blank deformation using the three material models, whereas Table 3 details the numerical and experimental values for each of the selected points at various cases.
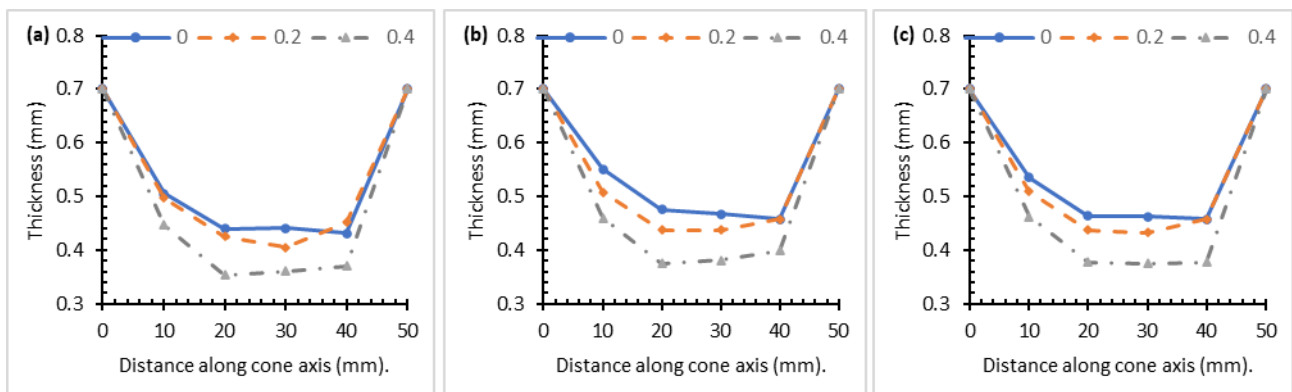

Figure 15. Thickness spatial variation at end of process as predicted by simulation using (**a**) GTN material model, (**b**) FFLD model, and (**c**) DD material model for different pressure settings.
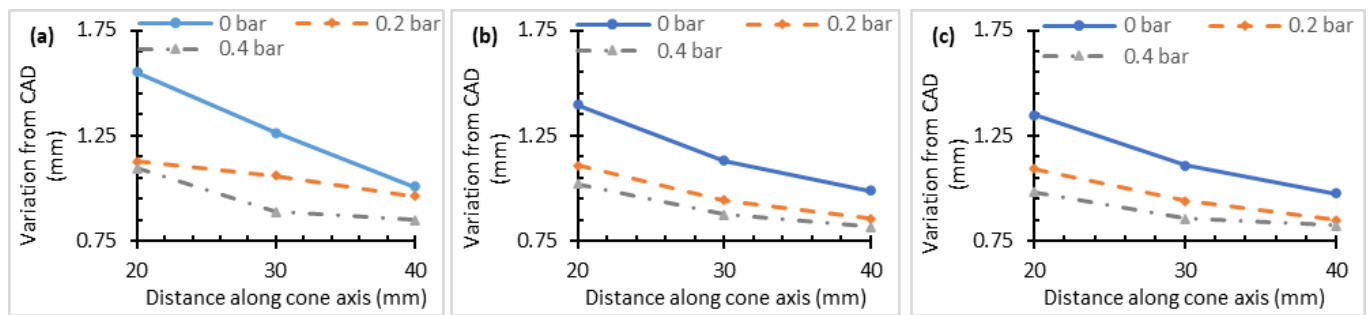
Figure 16. Variation from CAD at end of process as predicted by simulation using (**a**) GTN material model, (**b**) FFLD model, and (**c**) DD model for different pressure settings.

Table 3. Comparison of experimental and numerical results of various material models at different pressure settings.

Axial Depth (mm)	Experimental Results			FFLD			GTN			DD		
	0.0 bar	0.2 bar	0.4 bar	0.0 bar	0.2 bar	0.4 bar	0.0 bar	0.2 bar	0.4 bar	0.0 bar	0.2 bar	0.4 bar
Variation from CAD (mm)												
20	1.4	1.11	1.03	1.39	1.12	1.01	1.42	1.21	1.05	1.38	1.06	0.99
30	1.1	0.96	0.88	1.16	0.95	0.86	1.17	1.04	0.89	1.13	0.93	0.86
40	1.01	0.88	0.83	0.99	0.86	0.81	1.10	0.92	0.84	0.94	0.86	0.83
Thickness (mm)												
10	0.56	0.52	0.47	0.56	0.51	0.46	0.51	0.50	0.44	0.53	0.50	0.44
20	0.48	0.44	0.38	0.47	0.43	0.37	0.44	0.41	0.36	0.46	0.41	0.36
30	0.47	0.44	0.39	0.46	0.43	0.38	0.45	0.40	0.37	0.47	0.42	0.39
40	0.47	0.46	0.41	0.47	0.45	0.40	0.46	0.44	0.37	0.45	0.43	0.38

The FFLD material model showed the least variation with CAD, and it was within 90% agreement with experimental work, whereas the GTN and DD models agreed by 79% and 84%, respectively. The aforementioned results, which are summarised in Table 4, confirmed that the FFLD material model was the most accurate one for predicting material deformation and damage in the PA-SPIF process for DP600 steel metal sheets within the tested range of values.

Table 4. Summary of findings.

Characteristics	Material Model		
	FFLD	**DD**	**GTN**
No-fracture prediction	Yes	Yes	No
Thickness discrepancy up to (%)	3	6	10
Variation from CAD up to (%)	10	16	21

4. Conclusions

The current investigation compared three different material models for the finite-element analysis of pressure-assisted single-point incremental forming of the cold-rolled, dual-phase steel DP600. Experimental trials using 0.2 bar and 0.4 bar fluid pressures besides no fluid pressure (0 bar) showed good agreement with the simulation results with errors in deformed blank thickness and deformed geometry predictions of 3–11% and 10–21%, respectively. Based on the tested range of parameters and materials, the FFLD material model showed the least discrepancy with experiments, whereas the GTN model depicted the highest discrepancy in predicting thickness, geometry, and material

nonfracture condition. The GTN model ignores damage mechanisms due to shear, which might be vital in SPIF. The current investigation revealed the importance of a damage model in predicting deformation during SPIF using finite-element analysis; however, the plastic stress–strain constitutive model is of equal importance. Experimental uniaxial tension data were used in the current investigation for the constitutive stress–strain model; however, further testing at different temperatures, strain rates, and strain configurations (e.g., biaxial stretching) is needed for further improvements in modelling work.

References

1. Martins, P.A.F.; Bay, N.; Skjoedt, M.; Silva, M.B. Theory of Single Point Incremental Forming. *CIRP Ann.-Manuf. Technol.* **2008**, *57*, 247–252. [CrossRef]
2. Abdelhafeez, A.M.; Nemat-Alla, M.M.; El-Sebaie, M.G. FEA of Electromagnetic Forming Using a New Coupling Algorithm. *Int. J. Appl. Electromagn. Mech.* **2013**, *42*, 157–169. [CrossRef]
3. Abdelhafeez, A.M.; Nemat-Alla, M.M.; El-Sebaie, M.G. Finite Element Analysis of Electromagnetic Bulging of Sheet Metals. *Int. J. Sci. Eng. Res.* **2012**, *3*, 180–187.
4. Abdelhafeez, A.M.; Nemat-Alla, M.M.; El-Sebaie, M.G. FEA of Electromagnetic Forming Using a New Coupling Algorithm: Effects of Strain Hardening Properties and Anisotropy. *Int. J. Sci. Eng. Res.* **2014**, *5*, 1069–1075.
5. Emmens, W.C.; Sebastiani, G.; van den Boogaard, A.H. The Technology of Incremental Sheet Forming—A Brief Review of the History. *J. Mater. Processing Technol.* **2010**, *210*, 981–997. [CrossRef]
6. Peter, I.; Fracchia, E.; Canale, I.; Maiorano, R. Incremental Sheet Forming for Prototyping Automotive Modules. *Procedia Manuf.* **2019**, *32*, 50–58. [CrossRef]
7. Duflou, J.R.; Habraken, A.-M.; Cao, J.; Malhotra, R.; Bambach, M.; Adams, D.; Vanhove, H.; Mohammadi, A.; Jeswiet, J. Single Point Incremental Forming: State-of-the-Art and Prospects. *Int. J. Mater.* **2018**, *11*, 743–773. [CrossRef]
8. Scheffler, S.; Pierer, A.; Scholz, P.; Melzer, S.; Weise, D.; Rambousek, Z. Incremental Sheet Metal Forming on the Example of Car Exterior Skin Parts. *Procedia Manuf.* **2019**, *29*, 105–111. [CrossRef]
9. Behera, A.K.; de Sousa, R.A.; Ingarao, G.; Oleksik, V. Single Point Incremental Forming: An Assessment of the Progress and Technology Trends from 2005 to 2015. *J. Manuf. Processes* **2017**, *27*, 37–62. [CrossRef]
10. Kumar, A.; Gulati, V.; Kumar, P.; Singh, V.; Kumar, B.; Singh, H. Parametric Effects on Formability of AA2024-O Aluminum Alloy Sheets in Single Point Incremental Forming. *J. Mater. Res. Technol.* **2019**, *8*, 1461–1469. [CrossRef]
11. McAnulty, T.; Jeswiet, J.; Doolan, M. Formability in Single Point Incremental Forming: A Comparative Analysis of the State of the Art. *CIRP J. Manuf. Sci. Technol.* **2017**, *16*, 43–54. [CrossRef]
12. Kim, T.J.; Yang, D.Y. Improvement of Formability for the Incremental Sheet Metal Forming Process. *Int. J. Mech. Sci.* **2000**, *42*, 1271–1286. [CrossRef]
13. Ambrogio, G.; De Napoli, L.; Filice, L.; Gagliardi, F.; Muzzupappa, M. Application of Incremental Forming Process for High Customised Medical Product Manufacturing. *J. Mater. Processing Technol.* **2005**, *162–163*, 156–162. [CrossRef]
14. Cheng, Z.; Li, Y.; Xu, C.; Liu, Y.; Ghafoor, S.; Li, F. Incremental Sheet Forming towards Biomedical Implants: A Review. *J. Mater. Res. Technol.* **2020**, *9*, 7225–7251. [CrossRef]
15. Habibi, N.; Ramazani, A.; Sundararaghavan, V.; Prahl, U. Failure Predictions of DP600 Steel Sheets Using Various Uncoupled Fracture Criteria. *Eng. Fract. Mech.* **2018**, *190*, 367–381. [CrossRef]
16. Ham, M.; Jeswiet, J. Single Point Incremental Forming and the Forming Criteria for AA3003. *CIRP Ann.* **2006**, *55*, 241–244. [CrossRef]
17. Afonso, D.; de Sousa, R.A.; Torcato, R. Incremental Forming of Tunnel Type Parts. *Procedia Eng.* **2017**, *183*, 137–142. [CrossRef]
18. Moayedfar, M.; Leman, Z.; bin Baharudin, B.T.H.T. Incremental Sheet Forming (ISF) of AISI 316 Stainless Steel Sheet Using CNC Milling Machine. *AMR* **2014**, *939*, 322–327. [CrossRef]
19. Manco, G.L.; Ambrogio, G. Influence of Thickness on Formability in 6082-T6. *Int. J. Mater.* **2010**, *3*, 983–986. [CrossRef]
20. Mugendiran, V.; Gnanavelbabu, A. Comparison of FLD and Thickness Distribution on AA5052 Aluminium Alloy Formed Parts by Incremental Forming Process. *Procedia Eng.* **2014**, *97*, 1983–1990. [CrossRef]

21. Pereira Bastos, R.N.; Alves de Sousa, R.J.; Fernandes Ferreira, J.A. Enhancing Time Efficiency on Single Point Incremental Forming Processes. *Int. J. Mater.* **2016**, *9*, 653–662. [CrossRef]

22. Azevedo, N.G.; Farias, J.S.; Bastos, R.P.; Teixeira, P.; Davim, J.P.; Alves de Sousa, R.J. Lubrication Aspects during Single Point Incremental Forming for Steel and Aluminum Materials. *Int. J. Precis. Eng. Manuf.* **2015**, *16*, 589–595. [CrossRef]

23. Ham, M.; Jeswiet, J. Dimensional Accuracy of Single Point Incremental Forming. *Int. J. Mater.* **2008**, *1*, 1171–1174. [CrossRef]

24. Zhu, H.; Liu, L. Research the CNC Incremental Forming of Straight-Wall Parts Based on a Virtual Auxiliary Body. *J. Mater. Processing Technol.* **2021**, *288*, 116841. [CrossRef]

25. Zhu, H.; Wang, Y.; Kang, J. Research on Combinatorial Optimization of Multidirectional Sheet Postures for Forming Thickness Uniformity. *J. Mech. Sci. Technol.* **2020**, *34*, 4251–4261. [CrossRef]

26. Zhan, X.; Wang, Z.; Li, M.; Hu, Q.; Chen, J. Investigations on Failure-to-Fracture Mechanism and Prediction of Forming Limit for Aluminum Alloy Incremental Forming Process. *J. Mater. Processing Technol.* **2020**, *282*, 116687. [CrossRef]

27. Mirnia, M.J.; Vahdani, M.; Shamsari, M. Ductile Damage and Deformation Mechanics in Multistage Single Point Incremental Forming. *Int. J. Mech. Sci.* **2018**, *136*, 396–412. [CrossRef]

28. Chang, Z.; Chen, J. Investigations on the Deformation Mechanism of a Novel Three-Sheet Incremental Forming. *J. Mater. Processing Technol.* **2020**, *281*, 116619. [CrossRef]

29. Eyckens, P.; Belkassem, B.; Henrard, C.; Gu, J.; Sol, H.; Habraken, A.M.; Duflou, J.R.; Van Bael, A.; Van Houtte, P. Strain Evolution in the Single Point Incremental Forming Process: Digital Image Correlation Measurement and Finite Element Prediction. *Int. J. Mater.* **2011**, *4*, 55–71. [CrossRef]

30. Henrard, C.; Bouffioux, C.; Eyckens, P.; Sol, H.; Duflou, J.R.; Van Houtte, P.; Van Bael, A.; Duchêne, L.; Habraken, A.M. Forming Forces in Single Point Incremental Forming: Prediction by Finite Element Simulations, Validation and Sensitivity. *Comput. Mech.* **2011**, *47*, 573–590. [CrossRef]

31. Essa, K.; Hartley, P. An Assessment of Various Process Strategies for Improving Precision in Single Point Incremental Forming. *Int. J. Mater.* **2011**, *4*, 401–412. [CrossRef]

32. Esmaeilpour, R.; Kim, H.; Park, T.; Pourboghrat, F.; Mohammed, B. Comparison of 3D Yield Functions for Finite Element Simulation of Single Point Incremental Forming (SPIF) of Aluminum 7075. *Int. J. Mech. Sci.* **2017**, *133*, 544–554. [CrossRef]

33. Yan, Z.; Hassanin, H.; El-Sayed, M.A.; Eldessouky, H.M.; Djuansjah, J.; Alsaleh, A.N.; Essa, K.; Ahmadein, M. Multistage Tool Path Optimisation of Single-Point Incremental Forming Process. *Materials* **2021**, *14*, 6794. [CrossRef] [PubMed]

34. Li, W.; Shu, C.; Hassan, A.; Attallah, M.M.; Essa, K. Application of Machine Learning on Tool Path Optimisation and Cooling Lubricant in Induction Heating-Assisted Single Point Incremental Sheet Forming of Ti-6Al-4V Sheets. *Int. J. Adv. Manuf. Technol.* **2022**. [CrossRef]

35. Frikha, S.; Giraud-Moreau, L.; Bouguecha, A.; Haddar, M. Simulation-Based Process Design for Asymmetric Single-Point Incremental Forming of Individual Titanium Alloy Hip Cup Prosthesis. *Materials* **2022**, *15*, 3442. [CrossRef] [PubMed]

36. Wang, Y.; Wang, L.; Zhang, H.; Gu, Y.; Ye, Y. A Novel Algorithm for Thickness Prediction in Incremental Sheet Metal Forming. *Materials* **2022**, *15*, 1201. [CrossRef] [PubMed]

37. Pepelnjak, T.; Sevšek, L.; Lužanin, O.; Milutinović, M. Finite Element Simplifications and Simulation Reliability in Single Point Incremental Forming. *Materials* **2022**, *15*, 3707. [CrossRef]

38. Mulay, A.; Ben, S.; Ismail, S. Lubricant Selection and Post Forming Material Characterization in Incremental Sheet Forming. *IOP Conf. Ser. Mater. Sci. Eng.* **2020**, *967*, 012072. [CrossRef]

39. Diabb, J.; Rodríguez, C.A.; Mamidi, N.; Sandoval, J.A.; Taha-Tijerina, J.; Martínez-Romero, O.; Elías-Zúñiga, A. Study of Lubrication and Wear in Single Point Incremental Sheet Forming (SPIF) Process Using Vegetable Oil Nanolubricants. *Wear* **2017**, *376–377*, 777–785. [CrossRef]

40. Isik, K.; Gerstein, G.; Gutknecht, F.; Clausmeyer, T.; Nürnberger, F.; Maier, H.J.; Tekkaya, A.E. Investigations of Ductile Damage in DP600 and DC04 Deep Drawing Steel Sheets during Punching. *Procedia Struct. Integr.* **2016**, *2*, 673–680. [CrossRef]

41. Heibel, S.; Dettinger, T.; Nester, W.; Clausmeyer, T.; Tekkaya, A. Damage Mechanisms and Mechanical Properties of High-Strength Multiphase Steels. *Materials* **2018**, *11*, 761. [CrossRef] [PubMed]

42. Gatea, S.; Ou, H.; Lu, B.; McCartney, G. Modelling of Ductile Fracture in Single Point Incremental Forming Using a Modified GTN Model. *Eng. Fract. Mech.* **2017**, *186*, 59–79. [CrossRef]

43. Yu, H.L.; Jeong, D.Y. Application of a Stress Triaxiality Dependent Fracture Criterion in the Finite Element Analysis of Unnotched Charpy Specimens. *Theor. Appl. Fract. Mech.* **2010**, *54*, 54–62. [CrossRef]

44. Marciniak, Z.; Duncan, J.L.; Hu, S.J. *Mechanics of Sheet Metal Forming*, 2nd ed.; Butterworth-Heinemann: Oxford, UK, 2002; ISBN 978-0-7506-5300-8.